HHS Public Access

Author manuscript

Nat Biomed Eng. Author manuscript; available in PMC 2019 March 19.

Published in final edited form as:

Nat Biomed Eng. 2018 April ; 2(4): 254–264. doi:10.1038/s41551-018-0220-3.

Maps of in vivo oxygen pressure with submillimetre resolution and nanomolar sensitivity enabled by Cherenkov-excited luminescence scanned imaging

Brian W. Pogue[1,2], **Jinchao Feng**[3], **Ethan P. LaRochelle**[1], **Petr Bruza**[1], **Huiyun Lin**[4], **Rongxiao Zhang**[1], **Jennifer R. Shell**[1], **Hamid Dehghani**[5], **Scott C. Davis**[1,2], **Sergei A. Vinogradov**[6], **David J. Gladstone**[1,2,7], and **Lesley A. Jarvis**[2,7]

[1]Thayer School of Engineering, Dartmouth College, Hanover, NH, 03755

[2]Norris Cotton Cancer Center, Dartmouth-Hitchcock Medical Center, Lebanon NH 03756 USA.

[3]Faculty of Information Technology, Beijing University of Technology, Beijing, 100124 P. R. China.

[4]Key Laboratory of OptoElectronic Science and Technology for Medicine of Ministry of Education, Fujian Provincial Key Laboratory of Photonics Technology, Fujian Normal University, Fuzhou, 350007, P. R. China.

[5]School of Computer Science, University of Birmingham, Birmingham B152TT, UK.

[6]Department of Biochemistry and Biophysics, Perelman School of Medicine, University of Pennsylvania Philadelphia PA 19104 USA

[7]Department of Medicine, Geisel School of Medicine, Dartmouth College, Hanover NH 03755 USA.

Abstract

Low signal-to-noise ratios and limited imaging depths restrict the ability of optical-imaging modalities to detect and accurately quantify molecular emissions from tissue. Here, by using a scanning external X-ray beam from a clinical linear accelerator to induce Cherenkov excitation of luminescence in tissue, we demonstrate in vivo mapping of the oxygenation of tumours at depths of several millimetres, with submillimetre resolution and nanomolar sensitivity. This was achieved by scanning thin sheets of the X-ray beam orthogonally to the emission-detection plane, and by

Author Contributions

BP conceived the study and supervised all aspects of the work and drafted the manuscript; JF, HL, PB, ELR, RZ, JS each completed measurements and data analysis as well as designed the experiments and wrote initial parts of the manuscript and edited the entire manuscript. HD & SCD helped design and analyze the tomography work with JF, and each edited the manuscript. SV provided the molecular probe, provided advice on experimental design and data analysis and edited the manuscript. DJG & LAJ each contributed advice on radiotherapy design and data interpretation, as well as edited the manuscript.

Data Availability: The data that support the findings of this study are available within the paper and its supplementary information. Source datasets generated and analyzed during the study are available from the corresponding author upon request.

Code Availability: Image-reconstruction code was custom developed for this study, and is available for download in bulk through our website www.nirfast.org. Individual MATLAB routines are available from the corresponding author upon request.

Author Competing Interests

The authors declare no competing financial interests.

detecting the signal via a time-gated CCD camera synchronized to the radiation pulse. We also show with experiments using phantoms and with simulations that the performance of Cherenkov-excited luminescence scanned imaging (CELSI) is limited by beam size, scan geometry, probe concentration, radiation dose and tissue depth. CELSI might provide the highest sensitivity and resolution in the optical imaging of molecular tracers in vivo.

Introduction

Optical luminescence is the dominant preclinical imaging modality for the molecular probing of cells and tissue physiology, both in vitro and in vivo [1–3]. The sensitivity of optical detectors to small concentrations of molecular emitters and the ease of use of the detection technology make optical molecular imaging much more widely used than x-rays, ultrasound, nuclear medicine or magnetic resonance imaging (MRI). However, because of elastic scattering of light in tissue, the tissue depths accessible by optical imaging in vivo are fundamentally limited [4–6]. Although fluorescence and bioluminescence have been used extensively to elucidate intracellular signalling in vitro, their use in vivo is largely limited to bulk temporal kinetics, surface tissue imaging [7–9], or invasive/surgical measurements [7]. The inability to reconstruct the spatial origin of a detected photon generally limits non-invasive in vivo luminescent molecular imaging, where high spatial resolution has never been achieved beyond microscopy. Additionally, the decrease in signal intensity with depth into tissue is exponential, creating highly non-linear excitation during imaging, as illustrated in Figure 1(a).

Here, Cherenkov excited luminescence scanned imaging (CELSI) [10, 11] was used to sense luminescent molecular probes deep within tissue, utilizing megavolt (MV) x-ray radiation, and adopting an orthogonal excitation geometry that allows scanning the region of interest, similarly to the way fluorescent light sheet microscopy works [12], as shown in Figure 1(b). As the illuminated area is consistently at a known distance from the detector, this geometry maximises the signal to noise ratio, which tends to be the dominant factor in quantitative imaging of thick and optically turbid samples. Importantly, Cherenkov light of organic molecules is based upon the electronic energy level of the excitation beam. Thus, with high MV x-ray sheet illumination, the spatial targeting of x-rays can be optimally combined with biological organic probes [9] already widely used in animals for other imaging modalities and is translatable to humans. CELSI is intended as an optical imaging tool which can preserve the linearity of the emitted optical signal with depth, and not be overly affected by scatter dominance in tissue. Further illustration of the value of CELSI relative to other imaging modalities can be seen in the Supplementary Data, Figure S.1. The geometry used here is illustrated in Figure 1(c) and temporal and spatial parameters in Figure 1(d).

Cherenkov light is generated in tissue from the scatter-induced secondary electrons produced from x-rays, here generated by a therapeutic MV linear accelerator (LINAC), that interact with the dielectric media. The spectrum of Cherenkov light is broadband, peaks in the ultraviolet (UV), and decays in intensity (I) with a wavelength dependence of $I \sim 1/\lambda^2$, shown in Figure 1(e). Luminescence of the probe is therefore excited only within the volume that is directly in the path of the scanning radiation beam, Figure 1(b), so that all

luminescent signals detected by the intensified charge coupled device (ICCD) are considered as originating exclusively from within the pathway of the linear accelerator (LINAC) beam. This geometrical arrangement adopts some of the principles of directed excitation imaging tools, such as ultrasound, where depth-dependent attenuation correction can be applied to the data because of knowledge of the excitation or emission beam depth. The limiting factor remains the intensity attenuation with distance by diffusion scatter and absorption as the emitted light passes through the tissue. The luminescent probe used here Platinum Oxyphor G4 (PtG4) is optimized for oxygen sensing, with a luminescent lifetime in the range of 22–44 microseconds, and an emission wavelength in the near-infrared [13, 14], shown in Figure 1(e) & (f).

Deep-tissue Cherenkov excitation from ionizing radiation of isotopes can also excite molecular luminescence [15, 16], with the signal increasing proportionally to the emitted gamma ray energy. Similarly, radiation delivered by a medical LINAC generates Cherenkov emission within the treated tissue [17] and can be visualized for patient dosimetry studies [18], as well as excitation of molecular probes [19, 20]. This process can be utilized to excite fluorescent or phosphorescent probes in tissue to sense diagnostic molecular features, and has been demonstrated at low radiation doses [10], where high energy MV photons have the highest generation of Cherenkov, yet the lowest deposited dose level in tissue. The excitation light from Cherenkov is directed by the incident beam, and so the observation of emission need not be highly localized because the signal is backprojected along the line of the Cherenkov beam, and also enables attenuation correction to be readily applied to the signal, based upon the depth of the beam. Additionally, altering the orthogonal angle of the excitation beam to the collection plane allows some advantages in signal to background improvement, as used in thick tissue fluorescence microscopy[12, 21]. This geometry makes CELSI's approach to signal measurement much more useful for whole body imaging, as it eliminates the need to estimate the depth of the optical signal origin.

The aim of this work was to evaluate the potential for Cherenkov excited luminescence scanned imaging to directly sample partial pressure of oxygen (pO_2) in vivo for mammalian tissue, estimating the spatial resolution, depth and probe concentration sensitivity bounds, and estimate the signal to background values available for realistic tumor imaging applications.

Results

Beam Size:

By measuring total luminescence signal and considering prior information about position of the scanning beam, the distribution of optical signal along the direction of scanning can be recovered. In Figure 2(a)-(c), the possible beam geometries are illustrated, where the x-ray sheet can be shaped as a broad beam covering the entire tissue volume, as is commonly used in radiotherapy, or a 2 dimensional sheet of 5mm thickness, or a pencil beam, $5\times5mm^{2,}$ which can be raster scanned around the tissue. The benefit of a pencil beam would be the highest spatial resolution, in step sizes of 0.1mm, whereas the benefit of a broad sheet is the fast imaging acquisition. However, the choices here make a large impact on the image quality and signal strength. In Figure 2(d) a broad homogenous phantom was imaged with a

large square beam 100×100mm^2, and then by a thin sheet beam, 5×100 mm^2, and then a pencil beam, 5×5mm^2, as described in the Methods. The phantom used had an embedded luminescent square 10×10 mm^2, at depth within it, to test for signal recovery, and the contrast to noise ratio (CNR) was plotted in the region of interest (ROI_1) relative to the background (ROI_2), in Figure 2(e), for each of the three cases at different depths of the object.

Imaging Geometry:

Radiation beam energies are carefully chosen to reach specific depths in the body, and a set of beams from different gantry angles can be delivered to the patient from these planned entrance positions. In general, arbitrary angles and beam energies and dose values are chosen based upon an optimization algorithm to maximize dose to target regions and minimize dose to organs at risk of radiation damage. It is this flexibility of targeting which makes radiation-based excitation flexible for molecular imaging. The simplest angular geometries of orthogonal or lateral to the subject are shown in Figure 3(a) & (b), where the beam could be roughly orthogonal to the camera direction, for a sheet-like imaging, or aligned along it, for epi-illumination. While the range of possible angles is much more than this, these were chosen as the extremes of signal to background, as will be shown. A complete analysis of the effect of geometry upon singular value index, matrix condition number and matrix rank, for the Jacobian to be inverted, is shown in the Supplementary Information section, Figure S3, using coefficient values listed in Table S1.

The experimental set up was photographed and is shown in Figure 3(c) and (d), and a single image of a single 1mm diameter capillary filed with 500μM PtG4, at 5mm depth into a tissue phantom solution is shown for each geometry in Figure 3(e) and (f), respectively. The phantom was a broad flat liquid media 200×200mm^2, with the single luminescent capillary within it, and a scanned sheet beam was used to image with approximately 30 mGy per position of the beam. The color bar for each is the same and so the significantly higher background near 9,600 counts, leads to a contrast ratio of 1.14 and CBR value of 14% for the epi-illumination while the lower background near 2500 counts is seen for lateral illumination, leading to a contrast ratio of 3.5, and CBR of 220%. The higher background comes from the fact that the entire volume being imaged is being excited by Cherenkov, and so the signal comes from a mix of depths below the surface. Because of this observation, the lateral excitation geometry was used throughout most of the next experiments, providing a depth-selective excitation. A detailed analysis of the centroid position error and FWHM of recovered regions is shown in the Supplementary Information, in Figure S4

Dose, Concentration & Depth of Imaging:

The dominant factors affecting image recovery were explored systematically by varying one parameter at a time, as shown in Figure 4. The contrast to background ratio (CBR) was used as a metric of success, assessing how this varied with radiation dose delivered, concentration of PtG4 and depth of the object into the medium. The signal to background was defined as the ratio of the target relative to off the target. This figure of merit was chosen because CELSI is a background dominated imaging geometry, as are most luminescent and fluorescent imaging modalities [22]. CELSI of PtG4 in a 1mm diameter capillary was

assessed with different concentrations, depths (distance from capillary to phantom surface) and radiation doses. First using a fixed depth of 5mm, the concentrations range was varied logarithmically from 500 μM down to 0.78 μM inside a 1mm capillary, measuring CBR for a 1 second acquisition time for dose of 0.1 Gy, with the overlapping excitation volume being 3.9×10^{-6}L, making the number of moles used vary from 2.0 μmol down to 3 nmol. The results are shown in Figure 4(a), being monotonic in shape and reducing to a CBR of 1 at about 6–8 nmol. Next the CBR was tracked for a fixed concentration of 500 μM in the 1mm capillary, for 200 nmol in the excitation volume, varying the depth down to 20mm into the phantom, also using 0.1 Gy dose, as shown in Figure 4(b). This was monotonic with depth and appears to decrease near CBR=1 well beyond the 20mm depth. Finally, the variation with radiation pulses added together was studied at a target depth of 5mm and fixed concentration of 100 μM, or 2 nmol, showing monotonic dependence on dose in Figure 4(c), and decreasing to CBR of 1 at 2 radiation pulses, roughly equivalent to 1.67 mGy dose.

Scan Directions and Tomographic Reconstruction:

The direction and range of scan parameters in CELSI is quite large and three particular geometries were examined as analogous to other tomographic systems, and also used to compare CELSI to fluorescence tomography systems. First a study of fluorescence tomography as acquired in the epi-illumination geometry was completed, as well as transmission geometry. For this 1% noise was randomly added to the simulated forward data with either a single embedded object or the 3 objects, as shown in Figure 5. The stopping criteria for the iterative reconstruction was when either a change in projection error of less than 0.01% was reached between iterations or the maximum iteration number of 40 was achieved. A cartesian pixel basis is 30×30 squares was used in Figure 5, and shown in Figure 5(a) and (b) respectively with the test object shown, and reconstructed images in (d) and (e). The CELSI tomography image with lateral excitation and vertical detection is shown in the schematic (c) and reconstructed object in (f). In this case, CELSI signal is shown to improve signal detection, compared to epi-illumination fluorescence tomography and has higher contrast than transmission-based fluorescence tomography, with further numerical analysis of the Jacobian matrix improvement shown in the Supplementary Information section, Figure S3.

Next the range of possible scans available with CELSI was explored on how it would affect image recovery. As shown in Figure 5(g)-(i), the horizonal, vertical and diagonal aspects of a scan can more fully interrogate the image space, and reconstructed images for these three respective geometries are shown in (j)-(l), with recovery from the combination of all of them shown in (m). From these simulations it is obvious that the excitation line directions distort the recovered objects in the axial direction of the source-detector lines. As with all tomography applications, the larger the range of angles sampled, the better the image recovery can become, as shown in (m), better resolving the object in all directions. In this numerical study, 3 angles were used, as these were sufficient to resolve the 3 objects, yet in principle an unlimited number of angles could be used, limited only by the added dose given to the subject. So as in CT imaging, ultimately there is a dose-resolution-contrast tradeoff which dictates the imaging system performance.

Spatial Resolution:

Both experiments and simulation studies were completed to assess the ultimate limits to spatial resolution with optimized conditions. The reconstruction set up and convergence criteria were the same as in the previous section, but a larger pixel basis of 100×100 pixels was used to improve quality of reconstructed images in Figure 6 (and Figure S4). Simulation studies were carried out with varying depths and using a standard resolution test, varying the distance between two small objects as illustrated in Figure 6(a). The reconstructed images are shown in with intensity in terms of the reconvened yield, as defined by the PtG4 absorption coefficient multiplied by the quantum yield of emission. The results reveal that when the depth of inclusions was smaller than 5mm, the CELSI tomography has the ability to discriminate the two inclusions with edge-to-edge distance of 0.1 mm, as plotted in Figure 6(b). When the depth of inclusions was increased to 2.5cm, the two inclusions can be also discriminated with edge-to-edge distance but nearer 0.5 mm. When the depth of inclusions was increased to 3 cm, the two inclusions can be also discriminated with edge-to-edge distance but nearer 1.8 mm. The results show that CELSI tomography can yield high spatial resolution, but that this spatial resolution does degrade with depth into the medium, as expected, due to the loss of light penetration depth at these wavelengths. These CELSI results can be compared to Epi-FT and Full-FT results which have significantly lower spatial resolution, ranging from a few millimeters to beyond 10mm at depth of 15 and 25 mm into the medium. Figure 6(b) shows the minimum spatial resolution as a function of depth of inclusions. Epi-FT could not reconstruct the inclusions accurately when the depth of inclusions was deeper than 15 mm, therefore, the spatial resolution was not calculated.

Experimental studies were carried out to try and match the simulations but using a simpler geometry of a single capillary rod, positioned at 5mm into the tissue simulating phantom medium. A range of capillaries with diameters varying from 1mm down to 0.1mm were used and filled with PtG4 at 50 μM. The FWHM recovered was extracted and the observed FWHM is plotted against the true value in (d), showing nearly perfect linearity and matching the expected value of the smallest spatial resolution tested of 100 microns.

Rodent & Phantom Imaging for Sensitivity & Resolution Testing:

In order to verify that imaging in a complex tissue shape would be possible, the XFM-2 phantom was imaged with 1 mM PtG4 within 7 μL at the tip of the cylinder, for 7 nmol total PtG4, inserted into the central part of the body. For these mouse phantom experiments, 35 radiation sheets were used, and the vertical step of each sheet was approximately 0.52 mm. The 3D forward simulation mesh contained 18496 nodes, 93818 elements and 1712 boundary nodes, and the absorption and reduced scattering coefficients for excitation and emission were both set at μ_a=0.007 mm^{-1} & μ_s'=1.0 mm^{-1}. The reconstruction pixel basis was 25×25×25 voxels. The initial guess of regularization parameter was 10, and the convergence criteria to stop the iterative update was when a change in projection error was less than 0.01% between successive iterations or when the maximum number of iterations was reached at n=10. The remitted luminescence image from above is shown in Figure 7(a) with the Cherenkov beam in the plane of the tube, with the luminescence from the tube showing a blurry image, with full width at half maximum (FWHM) of 10.4×11.9 mm in the two orthogonal directions. This signal is super imposed on the white light image of the

mouse phantom. Reconstructed images are shown in the 3 orthogonal directions superimposed on CT scan images of the phantom (in grey scale). This recovery showed good localization and recovery of the shape as might be expected, shown in Figure 7(b), with FWHM values of the reconstructed inclusion of 5.1×5.1×4.7mm in total. Note that these dimensions are less than half of the FWHM values of planar projection imaging.

To further advance and test the performance of CELSI reconstruction, an in vivo experiment with breast cancer MDA-MB-231 xenograft tumors in a mouse was performed, with two separate injection sites on each of the mouse hind limbs. The mouse was injected with 50 nmol of PtG4 into the right side tumor and 10 nmol into the left side tumor, using a 50 μM stock solution. These doses were specifically chosen to be just above, and just below the detection threshold. Given the sizes of the tumors ($9\times9\times6mm^3\approx500mm^3$), these corresponded to approximately 0.4 nM and 0.10 nM, when averaged over the tumor volume. The mouse was imaged within 30 minutes of injection. The other experimental settings were identical to the phantom experiment. Figure 7(c) shows the CT scan of the animal, and (d) shows the acquired luminescent Maximum Intensity Projection image overlaid on the colorized CT scan, with this luminescence image showing very blurry localization, with FWHM of 18.9 × 14.8 mm in the two orthogonal directions. The CT images were used to generate a finite element mesh, and the optical properties of tissues in the mouse were estimated by average homogeneous values for a mouse, based upon published values [17].

For these in vivo experiments, the mouse was scanned with a sheet illumination procedure. A total of 19 irradiation sheets were used with a step between them of 0.8 mm. The forward simulation mesh contained 13185 nodes, 63852 elements and 3716 boundary nodes, and the absorption and scattering coefficients for excitation and emission were both set to μ_a=0.01 mm^{-1} and μ_s'=1.0 mm^{-1}. The voxel basis for reconstruction was 25×25×25 pixels, and the initial guess of regularization parameter is 1. The convergence criteria was when the projection error changed by less than 0.01% between successive iterations or the maximum iteration number of n=10 was reached. Figure 7(e), (f) and (g) show the CELSI tomography reconstructed results from the 3 orthogonal views of the body interior, with reconstructed CELSI data in red. The FWHM values of the reconstructed CELSI image was 2.2×2.2×1.9 mm^3. Note that these dimensions were 7–8 times smaller than with planar imaging. Thus, the tumor could be located accurately for the larger injected concentration, and the recovered size was substantially smaller than that achieved with planar diffuse imaging, as is conventional for either epi-fluorescence or Cherenkov-excited luminescence imaging without a scanned source. For the lower concentration tumor, the recovered regions were not visible above the noise level of the reconstructed image, illustrating the detection threshold was between 0.4 and 0.1 nM of total contrast agent in the scan volume at these tumor depths. The individual mouse shown is representative of the image quality and recovery possible within this concentration range, with a rotating view of the 3D volume in the *Supplementary Information*, video 1.

Rodent Imaging for pO_2 Sensing:

A final murine experiment to map out pO_2 was completed in mice with subcutaneous MDA-MB-231 tumors. A total of 4 animals and 8 tumors were imaged (2 tumors per animal), with

local injection of 50uL of 25uM PtG4, a total of 1.25 nmol per tumor. Each mouse was imaged while alive and then repeated at 30 minutes after sacrifice, where the drop in blood circulation and respiration causes a strong decrease in pO_2 values. Temperature was controlled using a heating pad, with alive mice at 35.1 +/− 1.5°C and dead mice at 31.9 +/− 1.2°C. The CELSI scan was completed vertically for these cases, with the video 2 of the experimental data capture included in supplementary data. Images of the luminescence at different delay times between linac pulse and emission captured are shown in Figure 8(a). These were used for each mouse to create images of lifetime (b) and with the Stern-Volmer equation, the tissue pO_2 (c). The summary of total lifetimes and pO_2 values are shown in (d) and (e), respectively, as box & whisker plots. The entire range of values in alive or dead animals do not overlap, indicating a significant difference in both lifetime and pO_2 (p-value < 0.001 for each). But more importantly the range of values is +/−30% in lifetime, and +/−40% in pO_2 value, as would be expected in heterogeneous tumors.

Discussion

Optical imaging of tissue has the potential for retrieving rich molecular information, but image recovery has been plagued by the scattering of light in tissue, which makes the signal nonlinear and affected by the shape of tissue, its optical properties, and its layers and regions. In practice, often the-signal-to noise ratio is unacceptably low, and doesn't provide appreciable depth into the tissue. CELSI can directly use high-energy radiotherapy beams to launch light directly into the tissue, and by the knowledge of where the light was placed, it can allow high-resolution recovery of luminescent sources. Although this approach to imaging has been introduced in the past few years [10, 11], the factors that dictate the performance have not been exhaustively analyzed, and nonlinear tomography has not been applied to fully vet the imaging-contrast recovery and spatial resolution. In this study, these issues have been fully examined, and the capabilities of this type of imaging can now be established for pO_2 imaging of tumors. A steered beam that provides localization of the excitation has inherent value, as it allows avoiding organs at risk and to multiplex the beam to multiple animals or multiple tissue volumes. The geometrical demonstrations of scanning explored in this study form the very basis of what can be done with a linac which is designed for highly conformal radiotherapy delivery.

The beam shape and angle of orientation have perhaps the largest effects upon the signal, with larger beam shapes having substantially larger signals and resulting contrast-to-background ratio, as shown in Figure 3(d), presumably based upon the fact that the light scatters and builds up within the tissue. Additionally, there is an output factor for the beam that reduces with smaller beam sizes as well, and so while smaller or thinner beams provide the best spatial resolution, as shown in Figure 3, they inherently provide the lower signal intensities as well. The direction of the beam relative to the camera, has perhaps the second most important factor, as a separation of the source from the surface being imaged inherently improves the observed contrast by suppressing background signals from surface tissues, as illustrated in the images of Figure 4. For these reasons, much of the work following these two initial studies focused around using the lateral beam geometry predominantly, and with a wide sheet of radiation, to maximize build up and light irradiance in the tissue. It is this localization of the excitation beam which provides the inherent value of CELSI relative to

isotope-based Cherenkov excitation studies[16, 23, 24]. In isotope-based molecular sensing, the sensitivity can be as high, or even higher, down to the sub-nanomole range, but the ability to reconstruct and localize the emission is not dictated by anything other than the detected emission. In CELSI imaging, the high precision knowledge of the beam allows both deconvolution and depth-dependent attenuation correction, leaving a reconstructed signal that is highly localized in space to better than 1-mm accuracy throughout the imaged volume of tissue.

Testing the key performance factors beyond these initial choices leads to a complex array of possible parameters. The radiotherapy dose, the probe concentration and the depth into the tissue each contribute to the detected signal in ways that would have a reciprocity, as illustrated in Figure 4(d). The imaging of luminescent targets is possible within the range of concentrations, doses and depths that are suitable for small-animal imaging. The molecule number ranges near a μM are typical for metabolites and higher concentration receptors, and the ability to resolve uptake within many millimeters of tissue is an important application in preclinical imaging. Within the volume of excitation, this corresponds to sensitivity needed near μmol to nmol levels. Radiation doses used here have been in the range of x-ray exams, so although the concept of using a linear accelerator for imaging appears dangerous from a radiation-safety perspective, it is critical to appreciate that this is done with very little dose delivered. Additionally, the radiation dose is selectively deposited to only where the scanned beam passes, so radiosensitive organs or dose-limiting volumes could be strategically avoided in an optimized scan.

A goal of this work has been to establish the feasibility of high spatial resolution several millimeters into the animal tissue. The spatial resolution is largely dictated by the precision in which the x-ray beam can be controlled, because the signal origin can be localized to where the beam excited the luminescent agent. The imaging tests, both experimentally and computationally, support the belief that the spatial resolution is in the range of 100–300 microns for objects as deep as 5mm into the tissue. Computationally, this spatial resolution appears to be resolvable down to 20mm of depth, and this fundamental limit is a fascinating goal for deep-tissue imaging, as it essentially implies achieving near microscopic resolution deep into tissue with optical imaging. This realization is fundamental in molecular sensing in deep tissue.

Finally, the tests used with mouse phantoms and mouse tumors, both demonstrate the localization concepts and how the accuracy of reconstruction is superior to diffuse tomography and to superficial MIP images of luminescence. This latter comparison to superficial imaging is important, because the vast majority of preclinical luminescence imaging is done with epi-illumination box systems, where a single superficial surface image of the animal is obtained. Being able to bring optical imaging to a significantly higher spatial resolution throughout the animal’s whole body would have a profound impact in molecular imaging. The mouse phantom tested the potential of CELSI imaging in conditions matching the geometry, size and average tissue optical properties of a mouse, where the reconstruction of the embedded 7ul of PtG4 was found to be spatially accurate. CELSI imaging was then tested in the heterogeneous tissue conditions of a mouse in vivo, addressing the lack of realistic internal heterogeneities in the phantom. The more detailed CELSI images of tumor

oxygenation shown in Figure 8 illustrate how this methodology can be used to sense tumor pO2, and potentially do this with high spatial resolution. The features mapped out in this figure have sub-millimeter lateral spatial resolution, showing the heterogeneity of the pO2 ranging from 40–90 mmHg, and confirms existing reported values for these tumours. The heterogeneity seen within intratumoral regions and between the tumors on the left and right presumably illustrate areas of high and low pO2 variation. Areas that are high are thought to be closer to blood vessels whereas those with lower pO2 are consistent with areas distal from blood supply. The ability to map pO2, pH and other features such as enzyme concentrations, protein expression, cell-receptor density or metabolites would be valuable in order to understand responses to therapy. This methodology will be most important for molecular features at higher spatial resolution, where tumor heterogeneity plays an important factor in therapeutic response.

In molecular imaging, there can be a separation between the imaging system's physical capabilities and the pharmacokinetics and localization of the biochemical targeting moiety. Yet, the value of a system is defined by the intersection of these two properties, where the physical resolution and contrast of the biochemical agent gets localized in biological features of the tissue. In the current realization of CELSI, the delivery was directly into solid tumors, avoiding the issue of plasma pharmacokinetics and tumor retention. As such, the chosen focus here has been largely technological development, combined with localized delivery of the agent to tumors. While there are clear limitations to this, the approach does still match with radiotherapy delivery as well, where the location of delivery is well planned as targeted to the treatment volume. As such, while the compound has its limitation at the site of injection, the knowledge of the oxygenation of these radiotherapy target sites is still of considerable value to radiation sensitization. Thus, we present the application of localized oxygen sensing with high resolution CELSI in this format with clear potential to be further advanced by improvements in the biotargeting of luminescent reporters. Recent studies have examined multiple agents for Cherenkov-excited sensitivity with fluorescence [14, 20, 25], and for the capability of detecting multiple emitters at the same time [26]. Yet in all of these studies, PtG4 has been shown to be the most sensitive probe in terms of lower limit on concentration. Also, with its design for oxygen sensitivity from quenching which is accessed by measurement of emission lifetime, it also provides one of the most practical tools for radiation therapy, where tissue oxygenation is known to be an important factor in therapy efficacy. However, there is also potential for other lifetime phosphor sensing agents such as pH [27, 28]

Outlook

Cherenkov Excited Luminescence Scanned Imaging (CELSI) allows pO_2 imaging at a spatial resolution close to 0.1 mm, detected at tissue depths of several millimeters through an intact living mouse, by using nanomolar levels of an oxygen-sensitive biological probe. X-ray beams from a linear accelerator are shaped into thin sheets to scan a field of view in arbitrary directions, and collect the Cherenkov emissions via time-gating of the captured luminescence, enabling molecular sampling of a number of agents relevant to the tissue microenvironment. The depths and signal recovery possible are suitable for applications using small-animal biomedical imaging models. Results from computer simulations and

experimental studies suggest that, when fully automated, CELSI may have the highest sensitivity and spatial resolution of any preclinical whole-body molecular-imaging system.

Methods

LINAC & Cherenkov Imaging:

Cherenkov was induced by a linear accelerator (Varian Linac 2100CD, Varian Medical System, Palo Alto, CA) based at the Norris Cotton Cancer Center, at Dartmouth-Hitchcock Medical Center. The LINAC multi-leaf collimator (MLC) provided high flexibility in shaping the output beam to make arbitrary shaped treatment fields. Leaves are 5mm wide in this LINAC and oriented in many long thin sheets that are controlled to move in and out of the output beam and can be controlled to a level of 0.1mm precision. The effect of beam shape on the signal to background recovered acquisition was studied with radiation beam sizes using a larger square beam 100×100 mm^2, a thin sheet beam of 5×100 mm^2, and a thin square pencil beam 5×5 mm^2 with a vial of PtG4 of 5 μM in the phantom. CELSI of capillary containing PtG4 500 μM was studied with radiation beam sizes of 40×40 mm^2 (epi-illumination) and 5×40 mm^2 (lateral illumination). Background was acquired with acquisition 500 μs trigger delay. Each of these were studied for epi-illumination imaging and then the thin sheet beam was also used for lateral sheet excitation, as will be shown, for optimal contrast. To maximize signal and minimize background interference, the room lights were shut off throughout these studies, and all lights in the room were masked off with black cloth and black tape, as shown in the photographs.

Luminescent Reporter & Tissue Phantoms:

NIR fluorescent phosphorescent probe PtG4 Oxyphor [27] was prepared in standard 1× PBS at 500 μM concentration. This reporter has a strong oxygen sensitivity as described in previous work. [13, 14], as well as emission in the near infrared wavelengths, and excitation across the visible spectrum, matching Cherenkov excitation. Previous studies have examined the comparison of luminescence from phosphors and fluorophores form Cherenkov excitation, and in all studies, time-gated luminescence provides superior signal to noise, because of the superior background suppression provided by time-gating technology [25, 29, 30].

The tissue simulating phantoms were prepared using 1% Intralipid© (Fresenius Kabi, Uppsala, Sweden). A capillary with 1 mm diameter of the probe at concentrations from 0.75 to 500 μM were placed inside the phantom at a depth which was varied between 2.5 to 20 mm from phantom surface being imaged. To study the dose efficacy for CELSI, the capillary containing the solution of the probe was irradiated with doses which varied from 360 pulses (approx. 5 Gy) down to 1 pulse (approx. 1.4 cGy) at 500 μM concentration and 5 mm depth.

Luminescence Imaging:

The imaging system consisted of a time-gated intensified CCD camera (ICCD, PI-MAX4 1024i, Princeton Instruments, USA), a commercial lens (Canon EF 135mm f/2L USM), and a tripod mounted. The camera was focused on the imaging field approximately 1 meter away. This distance was optimized through earlier studies where the signal to noise was

found optimal, by moving back from the field, to avoid too much backscatter generated noise. The time-gated ICCD camera was synchronized to the radiation pulses (approximately 3.25 μs duration, 360 Hz repetition rate) with the intensifier set as ×100 and turned on at a 3.5 μs or 500 μs gate delay following each radiation pulse for phosphorescence or background measurement, and luminescence generated during 50μs gate width was integrated via this ICCD. The display of images in emission were originally captured in counts per pixel, as read from the camera, and this has been calibrated to photons/mm^2/s by calibration of the number of photons detected per count, which was previously studied and found to be 95 counts read out at the CCD per one photon incident upon the ICCD photocathode. Similarly, the camera has 13×13 μm^2 pixels, and so this was converted from pixels to a mm^2 units.

Initial experiments focused on examining the signal to background issue, using a single 1mm inner diameter glass capillary tube (Hampton Research Corp, Glass number 50 capillaries, Aliso Viejo CA), filled with 500 microMolar PtG4, and imaging with the linac vs camera in two different geometries, as shown in Figure 3. In the vertical scan direction (also sometimes called epi-illumination geometry), where the linac and camera have the same perspective, higher background would be expected due to the high Cherenkov at the surface of the phantom, shown in Figure 3(c). Whereas when the linac beam was orthogonal to the camera direction, then Cherenkov is not produced at the surface, and background would expect to be lower as viewed by the camera, shown in Figure 3(d). These studies were carried out to experimentally verify this with a single capillary image.

Factors Affecting Contrast: Dose, Concentration, Depth:

The signal contrast in all imaging systems is a function of key parameters and so for CELSI it was hypothesized that these key factors would be linearly related to the radiation dose used, the concentration of probe present in the tissue, and the logarithm of the depth in which the target was located. The depth dependence on signal is likely more complex because of the light diffusion process, but might be expected to fall off over macroscopic distances with the effective attenuation coefficient of the medium, estimated by diffusion theory to be $\mu_{eff} = (3\mu_a\mu_s')^{1/2}$, where μ_a is the absorption coefficient and μ_s' is the transport scattering coefficient of the tissue. The dose delivered was varied by simple linear summation of the signal over more LINAC pulses, to effectively build up signal with delivered dose. The concentration of PtG4 was varied in solution within the embedded object, from 500 μM down to 0.78 μM using a 1mm capillary present at 5mm depth into the medium. The excitation volume of this was given by the overlap of the 5mm beam with the 1mm capillary, which was $V = \pi r^2 h = 3.9\times10^{-6}$ L.

The signal to background ratio was used as a metric of recovered accuracy in this study, with the simple calculation defined by the ratio of the average intensity values:

$$Signal\ to\ Background = \frac{< I_{ROI} >}{< I_B >}$$

Where I_{ROI} Is the mean pixel intensity in the region of interest (ROI) and the I_B is the mean pixel intensity in the background, outside the ROI. In some studies, the contrast to noise ratio was used as a metric, which was defined as:

$$CNR = \frac{< I_{ROI} > - < I_B >}{\sigma_B}$$

Where σ_B was defined as the standard deviation of intensities in the background region.

Spatial Resolution Assessment:

The spatial resolution of imaging was assessed with a range of glass capillary tubes of varying inner diameter, from 0.1mm up to 1.0mm (Hampton Research Corp, Glass number 50 capillaries, Aliso Viejo CA). These tubes were placed into tissue simulating phantom at 5mm depth one by one, and all were filled with 50 μM PtG4 to provide a high contrast target for resolution assessment. The sheet radiation beam was scanned laterally across the tube, to vary the signal with position, and the linescan full width at half maximum (FWHM) was recovered for each capillary experiment.

Computed Tomography Recovery:

CELSI data can be scanned for different beam angles and the performance expected varies considerably based upon these choices. The range of options is so large that experimental study of these is prohibitive, and so a series of computer simulations were carried out, in particular to compare CESLI images to diffuse fluorescence tomography images where traditional light excitation is used as compared to Cherenkov excitation. Additionally, different combinations of scanning angles and different depths and sizes of objects could be simulated much more quickly than carrying out all the experiments. The computer simulations were carried out in the NIRFAST software package (available at www.nirfast.org), used to model light transport in tissue, and carry out regularized iterative reconstruction of the luminescent reporter in the medium. The recovery of the reporter was in terms of units of luminescent yield, $\eta\mu_{af}$, where η is the reporter quantum yield for phosphorescence emission and μ_{af} is the absorption coefficient of the reporter (see Supplementary Information for further explanation of the theory). This quantity is a direct report of the amount of light produced per unit volume. To assess spatial resolution of CELSI tomography, a classic resolution test was performed with two small inclusions and varying the spatial distance between them and assessing when they could not be resolved as separate objects. The edge-to-edge distance was varied from 0.1 mm to 5 mm, in the plausible range of limiting spatial resolutions given the physical constraints of the LINAC MLCs used. The yield contrast of inclusion was set as 10:1. A finer mesh with 6161 nodes and 12000 linear triangular elements was used in reconstruction. Inspired by the results of combining of scan modes, the following reconstructions were performed by summing up scan modes.

Animal Phantom Imaging:

In order to assess performance in a more complex tissue geometry, a commercially available mouse phantom was used (Xfm-2, PerkinElmer Health Sciences, Waltham MA), using rod of material inserted which was filled with 1 mM PtG4, in 7 μL (7 nmol). This phantom has tissue optical properties within the NIR wavelengths 650–800nm, approximated by μ_a=0.003–0.008 mm^{-1} and $\mu_s/$=1.5–0.9 mm^{-1} (manufacturer supplied data sheet). This phantom was crated for phantom studies which would allow imaging in a realistic tissue volume and geometry that directly mimics the shape and absorption and reduced scattering coefficient values representative of murine tissue. The CELSI imaging was carried out with lateral beam excitation and vertically oriented emission capture, using a long lifetime gate on the camera, to sync out the Cherenkov light and noise, and maximize luminescence emission detection. X-ray tomography was completed on the IVIS Spectrum CT (PerkinElmer Inc, Hopkington MA) with the full field of view 120×120×30mm^3, with a 150 μm voxel scan acquired in 90 seconds.

Tumor Cell Lines:

MDA-MB-231 cells were purchased directly from ATCC as a confirmed cell type and mycoplasma free, no further testing was performed, and the cells lines are not listed in the ICLAC database of cross-contaminated or misidentified cell lines. Cells were grown in culture media in an incubator at 37°C in DMEM with 10% (v/v) Fetal Bovine Serum (FBS) and 1% penicillin-streptomycin. When ready for use, cells were trypsonized, counted, spun down into a slurry, and used for inoculation into animals.

Animal Studies:

All animal procedures were approved by the Dartmouth Institutional Animal Care and Use Committee, and the studies here were carried out in compliance with these approved procedures. Nude female mice were purchased at 6 weeks of age from Charles River Labs. After a week of acclimatization, animals were used for injections of 10^5 cells under the skin on each flank of the mouse in individual 0.050 mL injections. After approximately 3 weeks of growth, when a tumor with an average of 6mm diameter tumor was observed on both flanks, then the animals were used for imaging studies. All mice were under general anesthesia of inhaled isofluorane at 1.5% in flowing air through a nose cone throughtout imaging. For the tomography study, to demonstrate the detection level, a total of 0.5ml of PtG4 was directly injected into the tumors of a mouse, with one concentration of 50 nmol into one tumor and 10 nmol into the other tumor. This animal was imaged by 3D CELSI tomography at 30 minutes after injection, and then again imaged in the IVIS Spectrum CT system for x-ray tomography. The x-ray scan utilized 50 kVp standard 150 micron resolution imaging of the mouse in a 12×12×3cm^3 field size. In further pO_2 imaging studies, a cohort of 4 mice were used with a tumor in each flank (2 tumors per mouse, for n=8 tumors) and used for imaging when the average dimension diameter was 6mm as measured over the two orthogonal axes.

Statistical Analysis:

The differences between the alive and dead conditions, as displayed in Figure 8, with n=8 paired samples each was established by a two tailed students t-test, with alpha=0.05, and resulting p-value < 0.001. These indicate that both in lifetime as well as pO_2, there are significant differences between the values of the animals in the two conditions. However more pertinent to the value of the study is the observation of the total range of values, presented as a % of the median value. The figures 8(d) & (e) were generated using Python 3.4.3 with the library matplotlib 2.0.0. The function used to make the box plot is called boxplot available at this link: (https://matplotlib.org/api/_as_gen/matplotlib.pyplot.boxplot.html). The box extends from the lower to the upper quartile values of the data, with a line at the median. The whiskers extend from the box to show the range of the data. Flier points are those past the end of the whiskers.

Supplementary Material

Refer to Web version on PubMed Central for supplementary material.

Acknowledgments

This work has been funded by the Congressionally Directed Medical Research Program for Breast Cancer Research Program, U.S. Army USAMRAA contract W81XWH-16-1-0004 and National Institutes of Health research grant R01 EB024498 and R01 EB018464.

References

1. Hoebe RA, Van Oven CH, Gadella TW, Jr., Dhonukshe PB, Van Noorden CJ, and Manders EM, Controlled light-exposure microscopy reduces photobleaching and phototoxicity in fluorescence live-cell imaging. Nat Biotechnol, 2007 25(2): p. 249–53. [PubMed: 17237770]
2. Brismar H and Ulfhake B, Fluorescence lifetime measurements in confocal microscopy of neurons labeled with multiple fluorophores. Nat Biotechnol, 1997 15(4): p. 373–7. [PubMed: 9094141]
3. Nie S, Chiu DT, and Zare RN, Probing individual molecules with confocal fluorescence microscopy. Science, 1994 266(5187): p. 1018–21. [PubMed: 7973650]
4. Zipfel WR, Williams RM, Christie R, Nikitin AY, Hyman BT, and Webb WW, Live tissue intrinsic emission microscopy using multiphoton-excited native fluorescence and second harmonic generation. Proc Natl Acad Sci U S A, 2003 100(12): p. 7075–80. [PubMed: 12756303]
5. Bjorn S, Ntziachristos V, and Schulz R, Mesoscopic epifluorescence tomography: reconstruction of superficial and deep fluorescence in highly-scattering media. Opt Express, 2010 18(8): p. 8422–9. [PubMed: 20588688]
6. Georgakoudi I, Jacobson BC, Van Dam J, Backman V, Wallace MB, Muller MG, Zhang Q, Badizadegan K, Sun D, Thomas GA, Perelman LT, and Feld MS, Fluorescence, reflectance, and light-scattering spectroscopy for evaluating dysplasia in patients with Barrett's esophagus. Gastroenterology, 2001 120(7): p. 1620–9. [PubMed: 11375944]
7. Mittapalli RK, Manda VK, Bohn KA, Adkins CE, and Lockman PR, Quantitative fluorescence microscopy provides high resolution imaging of passive diffusion and P-gp mediated efflux at the in vivo blood-brain barrier. J Neurosci Methods, 2013 219(1): p. 188–95. [PubMed: 23916719]
8. Leblond F, Davis SC, Valdes PA, and Pogue BW, Pre-clinical whole-body fluorescence imaging: Review of instruments, methods and applications. J Photochem Photobiol B, 2010 98(1): p. 77–94. [PubMed: 20031443]
9. Pogue BW, Optics in the Molecular Imaging Race. Optics & Photonics News, 2015 Sept.: p. 25–31.

10. Zhang R, D'Souza A V, Gunn JR, Esipova TV, Vinogradov SA, Glaser AK, Jarvis LA, Gladstone DJ, and Pogue BW, Cherenkov-excited luminescence scanned imaging. Opt Lett, 2015 40(5): p. 827–30. [PubMed: 25723443]
11. Bruza P, Lin H, Vinogradov SA, Jarvis LA, Gladstone DJ, and Pogue BW, Light sheet luminescence imaging with Cherenkov excitation in thick scattering media. Opt Lett, 2016 41(13): p. 2986–9. [PubMed: 27367082]
12. Chen BC, Legant WR, Wang K, Shao L, Milkie DE, Davidson MW, Janetopoulos C, Wu XS, Hammer JA, 3rd, Liu Z, English BP, Mimori-Kiyosue Y, Romero DP, Ritter AT, Lippincott-Schwartz J, Fritz-Laylin L, Mullins RD, Mitchell DM, Bembenek JN, Reymann AC, Bohme R, Grill SW, Wang JT, Seydoux G, Tulu US, Kiehart DP, and Betzig E, Lattice light-sheet microscopy: imaging molecules to embryos at high spatiotemporal resolution. Science, 2014 346(6208): p. 1257998. [PubMed: 25342811]
13. Spencer JA, Ferraro F, Roussakis E, Klein A, Wu J, Runnels JM, Zaher W, Mortensen LJ, Alt C, Turcotte R, Yusuf R, Cote D, Vinogradov SA, Scadden DT, and Lin CP, Direct measurement of local oxygen concentration in the bone marrow of live animals. Nature, 2014 508(7495): p. 269–73. [PubMed: 24590072]
14. Zhang R, Davis SC, Demers JL, Glaser AK, Gladstone DJ, Esipova TV, Vinogradov SA, and Pogue BW, Oxygen tomography by Cerenkov-excited phosphorescence during external beam irradiation. J Biomed Opt, 2013 18(5): p. 50503. [PubMed: 23644902]
15. Dothager RS, Goiffon RJ, Jackson E, Harpstrite S, and Piwnica-Worms D, Cerenkov radiation energy transfer (CRET) imaging: a novel method for optical imaging of PET isotopes in biological systems. PLoS One, 2010 5(10): p. e13300. [PubMed: 20949021]
16. Thorek DL, Ogirala A, Beattie BJ, and Grimm J, Quantitative imaging of disease signatures through radioactive decay signal conversion. Nat Med, 2013 19(10): p. 1345–50. [PubMed: 24013701]
17. Axelsson J, Glaser AK, Gladstone DJ, and Pogue BW, Quantitative Cherenkov emission spectroscopy for tissue oxygenation assessment. Opt Express, 2012 20(5): p. 5133–42. [PubMed: 22418319]
18. Jarvis LA, Zhang R, Gladstone DJ, Jiang S, Hitchcock W, Friedman OD, Glaser AK, Jermyn M, and Pogue BW, Cherenkov video imaging allows for the first visualization of radiation therapy in real time. Int J Radiat Oncol Biol Phys, 2014 89(3): p. 615–22. [PubMed: 24685442]
19. Axelsson J, Davis S, Gladstone D, and Pogue B, Cerenkov emission induced by external beam radiation stimulates molecular fluorescence. Med Phys, 2011 38(7): p. 4127–4132. [PubMed: 21859013]
20. Demers JL, Davis SC, Zhang R, Gladstone DJ, and Pogue BW, Cerenkov excited fluorescence tomography using external beam radiation. Opt Lett, 2013 38(8): p. 1364–6. [PubMed: 23595486]
21. Keller PJ, Schmidt AD, Wittbrodt J, and Stelzer EH, Reconstruction of zebrafish early embryonic development by scanned light sheet microscopy. Science, 2008 322(5904): p. 1065–9. [PubMed: 18845710]
22. Keereweer S, Sterenborg HJ, Kerrebijn JD, Van Driel PB, Baatenburg de Jong RJ, and Löwik CW, Image-guided surgery in head and neck cancer: current practice and future directions of optical imaging. Head Neck, 2012 34(1): p. 120–126. [PubMed: 21284051]
23. Mitchell GS, Gill RK, Boucher DL, Li C, and Cherry SR, In vivo Cerenkov luminescence imaging: a new tool for molecular imaging. Philos Transact A Math Phys Eng Sci, 2011 369(1955): p. 4605–19.
24. Das S, Thorek DL, and Grimm J, Cerenkov imaging. Adv Cancer Res, 2014 124: p. 213–34. [PubMed: 25287690]
25. Lin H, Zhang R, Gunn JR, Esipova TV, Vinogradov S, Gladstone DJ, Jarvis LA, and Pogue BW, Comparison of Cherenkov excited fluorescence and phosphorescence molecular sensing from tissue with external beam irradiation. Phys Med Biol, 2016 61(10): p. 3955–68. [PubMed: 27120085]
26. Dsouza A, Lin H, Gunn JR, Gladstone DJ, Jarvis LA, and Pogue BW, Cherenkov-excited multi-fluorophore sensing in tissue-simulating phantoms and in vivo. Radiat. Res, 2017: p. (in press).

27. Esipova TV, Karagodov A, Miller J, Wilson DF, Busch TM, and Vinogradov SA, Two new “protected” oxyphors for biological oximetry: properties and application in tumor imaging. Anal Chem, 2011 83(22): p. 8756–65. [PubMed: 21961699]

28. Czupryna J, Kachur AV, Blankemeyer E, Popov AV, Arroyo AD, Karp JS, and Delikatny EJ, Cerenkov-specific contrast agents for detection of pH in vivo. J Nucl Med, 2015 56(3): p. 483–8. [PubMed: 25655631]

29. Holt RW, Zhang R, Esipova TV, Vinogradov SA, Glaser AK, Gladstone DJ, and Pogue BW, Cherenkov excited phosphorescence-based pO2 estimation during multi-beam radiation therapy: phantom and simulation studies. Phys Med Biol, 2014 59(18): p. 5317–28. [PubMed: 25146556]

30. Zhang R, Glaser A, Esipova TV, Kanick SC, Davis SC, Vinogradov S, Gladstone D, and Pogue BW, Cerenkov radiation emission and excited luminescence (CREL) sensitivity during external beam radiation therapy: Monte Carlo and tissue oxygenation phantom studies. Biomed Opt Express, 2012 3(10): p. 2381–94. [PubMed: 23082280]

31. Lehmann S, Perera R, Grimm HP, Sam J, Colombetti S, Fauti T, Fahrni L, Schaller T, Freimoser-Grundschober A, Zielonka J, Stoma S, Rudin M, Klein C, Umana P, Gerdes C, and Bacac M, In Vivo Fluorescence Imaging of the Activity of CEA TCB, a Novel T-Cell Bispecific Antibody, Reveals Highly Specific Tumor Targeting and Fast Induction of T-Cell-Mediated Tumor Killing. Clin Cancer Res, 2016 22(17): p. 4417–27. [PubMed: 27117182]

32. Tang Q, Wang J, Frank A, Lin J, Li Z, Chen CW, Jin L, Wu T, Greenwald BD, Mashimo H, and Chen Y, Depth-resolved imaging of colon tumor using optical coherence tomography and fluorescence laminar optical tomography. Biomed Opt Express, 2016 7(12): p. 5218–5232. [PubMed: 28018738]

33. Kepshire DS, Gibbs-Strauss SL, O’Hara JA, Hutchins M, Mincu N, Leblond F, Khayat M, Dehghani H, Srinivasan S, and Pogue BW, Imaging of glioma tumor with endogenous fluorescence tomography. J Biomed Opt, 2009 14(3): p. 030501. [PubMed: 19566285]

34. Dehghani H, Eames ME, Yalavarthy PK, Davis SC, Srinivasan S, Carpenter CM, Pogue BW, and Paulsen KD, Near infrared optical tomography using NIRFAST: Algorithm for numerical model and image reconstruction. Commun Numer Methods Eng, 2008 25(6): p. 711–732. [PubMed: 20182646]

35. Jermyn M, Ghadyani H, Mastanduno MA, Turner W, Davis SC, Dehghani H, and Pogue BW, Fast segmentation and high-quality three-dimensional volume mesh creation from medical images for diffuse optical tomography. J Biomed Opt, 2013 18(8): p. 86007. [PubMed: 23942632]

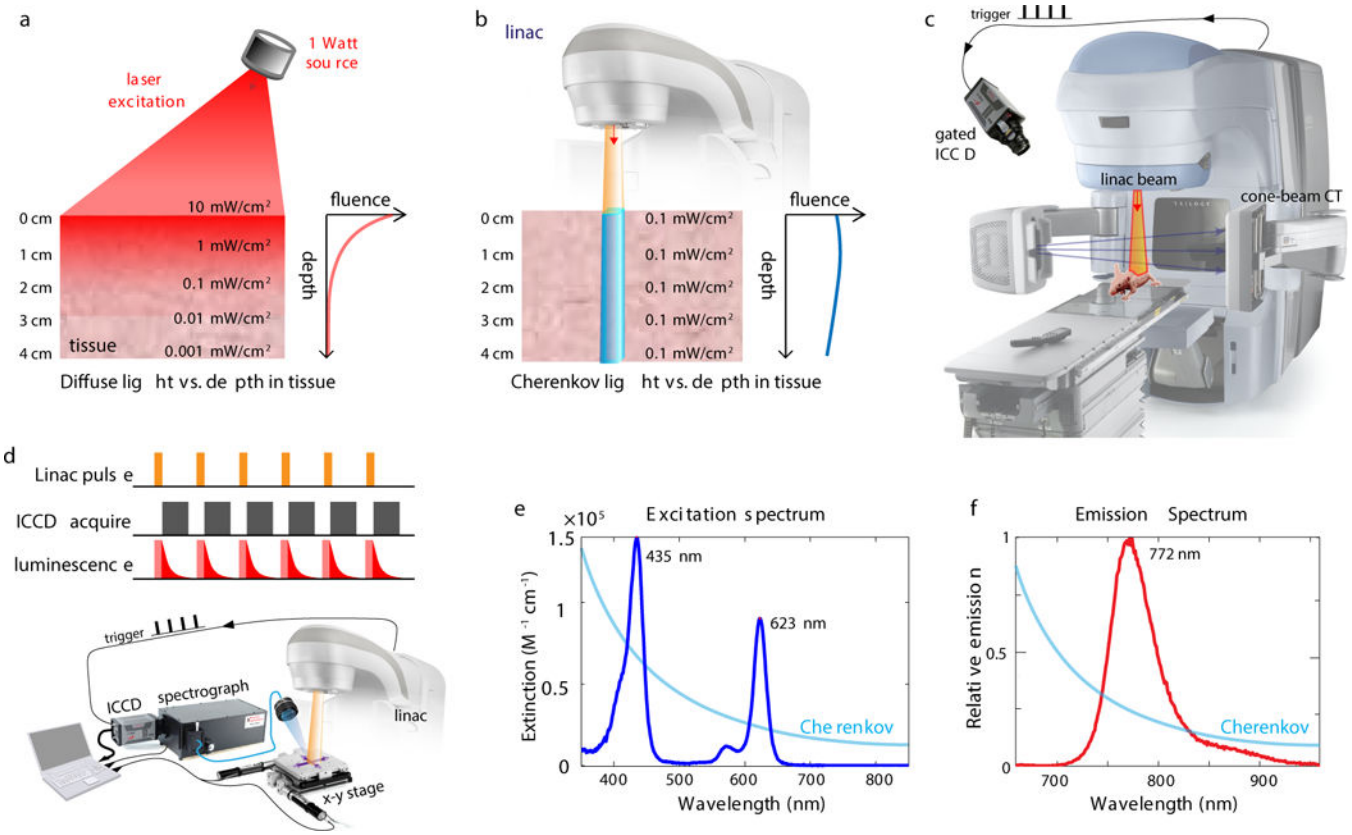

Figure 1.

A comparison of the excitation fluence loss with depth into tissue for (a) laser/LED excitation and (b) Cherenkov excitation generated within the tissue from a LINAC radiation beam. The diagram of the experimental setup is shown (c) with measurement devices. In (d) a raster scan approach to image measured by the ICCD is shown with gated emission detected by a spectrometer system. In (e) the absorption and (f) the luminescence emission spectra are shown for PtG4, with peak wavelengths labeled, and overlaid with the Cherenkov spectrum (blue) from single solution scans. The structure of PtG4 is illustrated in the Supplementary Information, Figure S2.

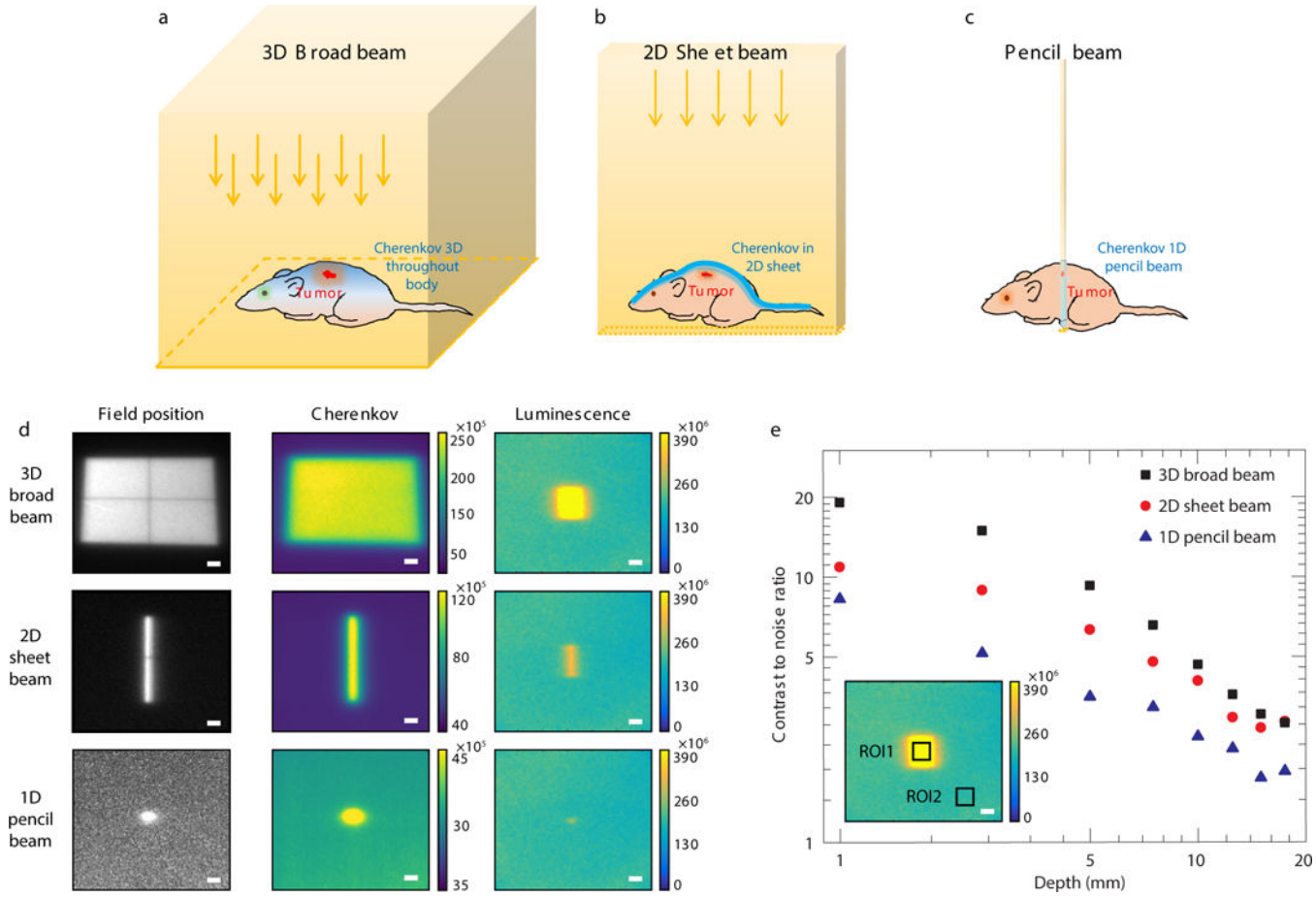

Figure 2.

The configuration of the radiation beam shape and region of the tissue where Cherenkov would be generated by a (a) single broad beam throughout the 3D volume of the animal, or (b) in a 2D sheet beam, or (c) in a 1D pencil beam. These geometric choices each affect the signal to noise possible with CELSI, and hence the sensitivity of other parameters such as minimum concentration and depth of imaging feasible and acquisition time. Images of the field light, Cherenkov emission on a phantom and the luminescence from a single square target in the phantom are shown in (d) for the geometries in (a)-(c), with duplicate images taken in separate imaging sessions showing nearly identical image quality. The contrast to noise ratio (CNR) of the target relative to the background is shown in (e) as measured by individual scans, where each data point represents an individual acquisition. The units for the color bars on images in (d) and inset in (e) are in detected photons/cm^2/s and a 1cm scale bar is in the bottom right corner of each panel.

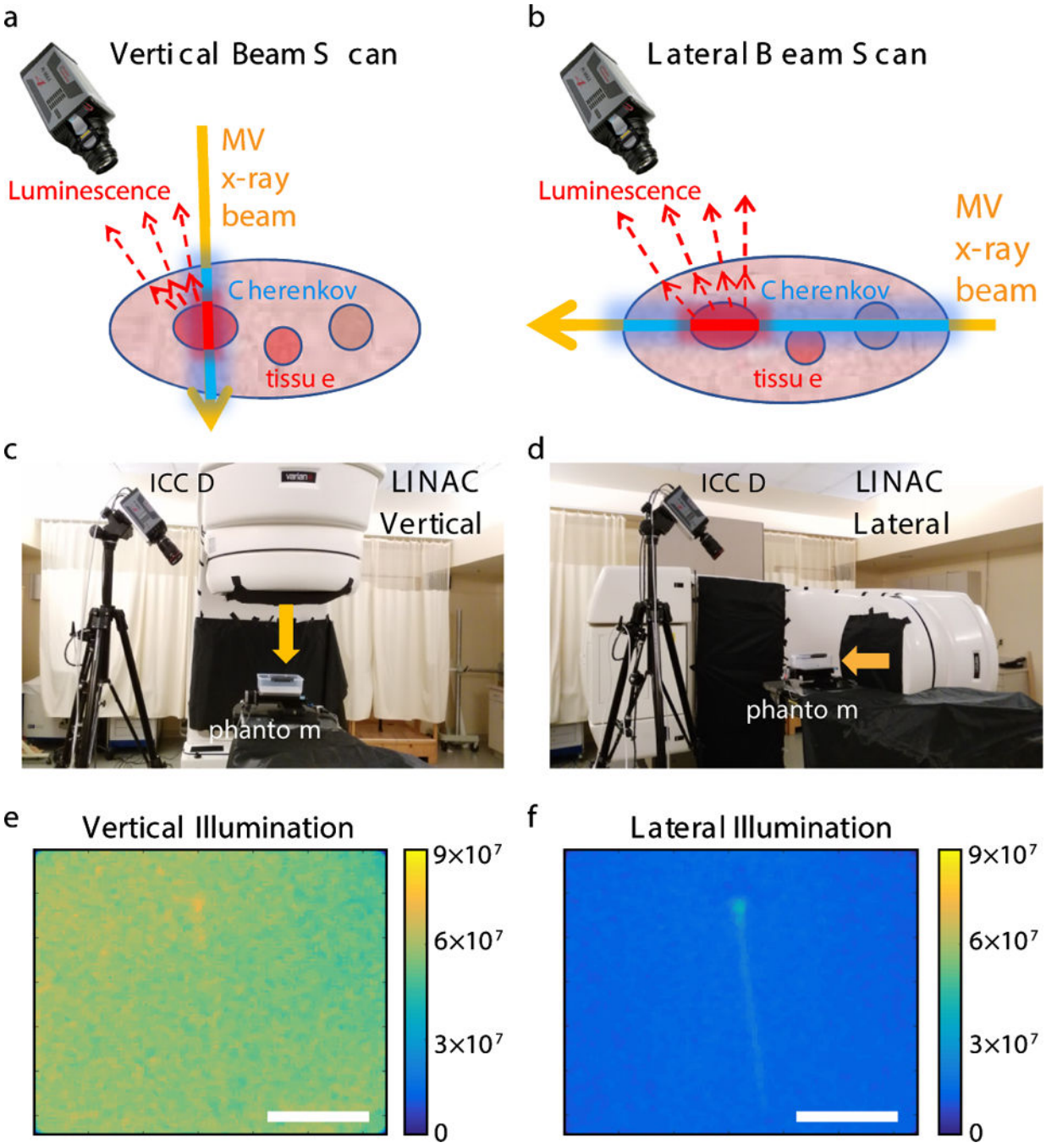

Figure 3.

The geometry of imaging camera relative to X-ray beam entrance position is shown in (a) an vertical (or epi-illumination) scan, and (b) a lateral sheet scan. Photographs of the LINAC-camera set up for (c) vertical and (d) orthogonal camera and LINAC beam, similar to schematics (a) and (b). Single frame images of PtG4 luminescence from one capillary within a broad tissue phantom are shown in (e) and (f) for these geometries, respectively, with color bars on the same scale for the two representing the full range available on the camera. These representative single images illustrate the high background and hence poorer contrast from

the epi-illumination geometry, as seen from an individual snapshot. The signal to background values are 15% for (e) and 220% for (f) above the background level. The units for the color bars on images in (e) and (f) are in detected photons/cm^2/s and 5mm scale bar is shown in the bottom right of each panel.

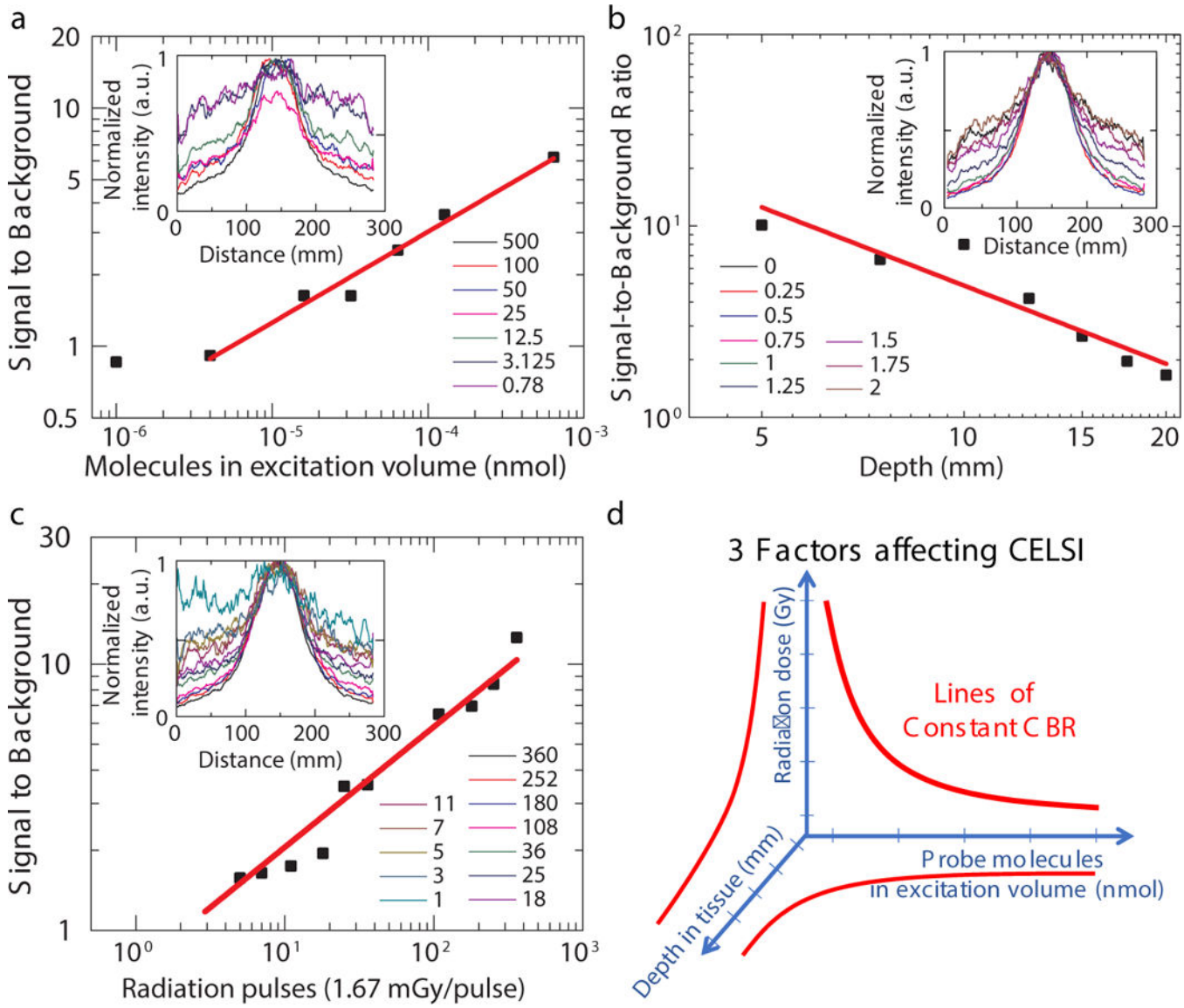

Figure 4.

Signal to background ratio measurements from PtG4 contained within a 1mm capillary with (a) different concentrations in the physiologically relevant range, (b) varying depth between the capillary wall to the surface of the phantom being imaged, and (c) varying radiation dose between 1 and 500 radiation pulses, with 1.67mGy/pulse. In each graph, the line scan raw data is inset. Each individual data point represents extraction of signal to background for a single scan of a test object, with varying conditions as shown in the x-axes. The red lines in each graph illustrate the linear trendline of the data on the log-log plots. In (d) the factors affecting CELSI signal strength are schematically illustrated as being reciprocal in their effect upon signal to background, illustrated by the red lines of constant value.

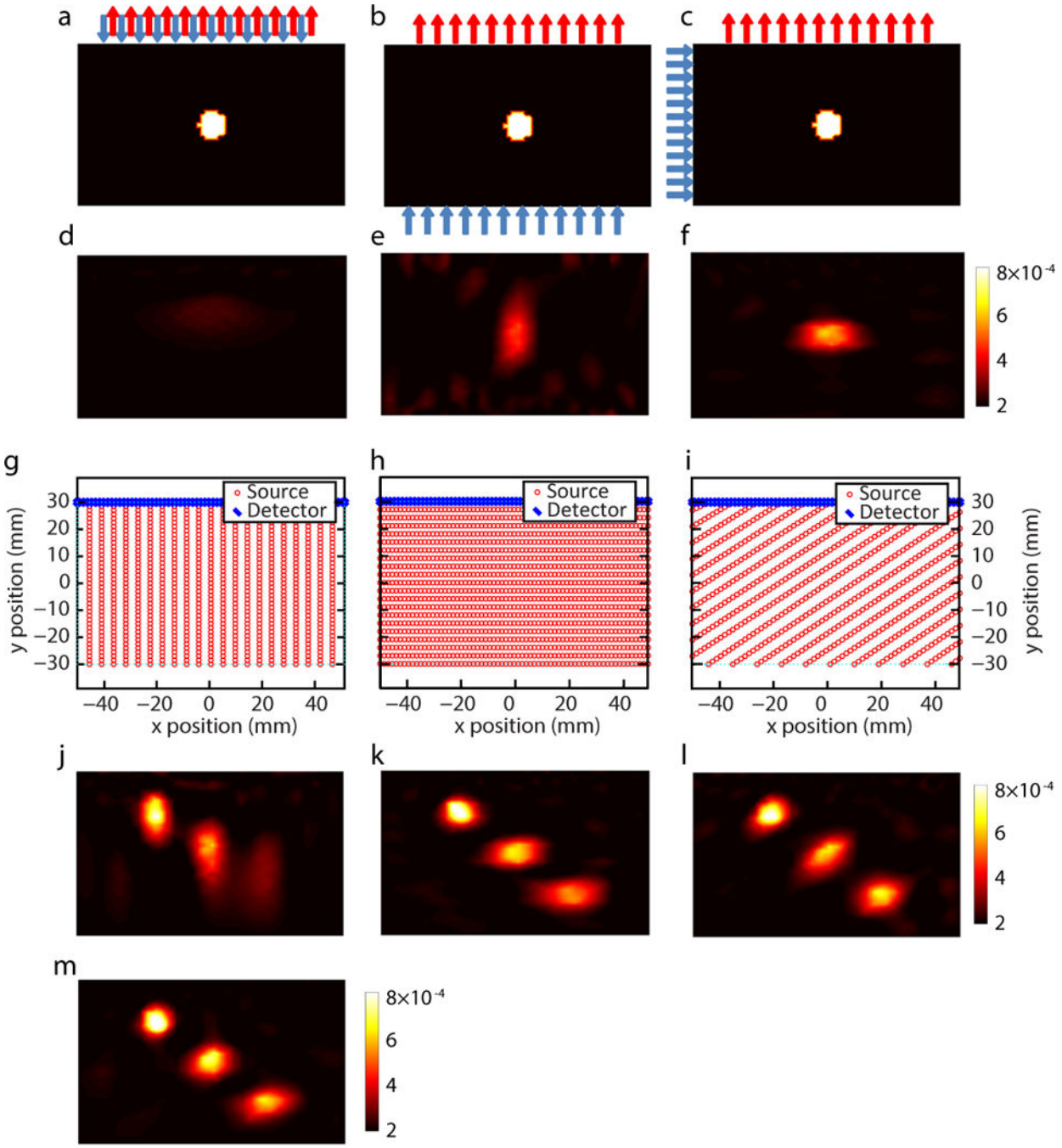

Figure 5.

Source and detector placement used for (a) the Epi-fluorescence tomography (Epi-FT), (b) the Full-FT, and (c) the lateral excitation CELSI with tomographic reconstruction. The blue arrows represent the source locations, and the red arrows denote the detector locations. Reconstructed luminescence distributions corresponding to the three geometries shown in Figure 2(a)-(c), for (d) the Epi-FT, (e) the Full-FT, and (f) the CELSI. Three angles of scanning for CELSI were examined as illustrated in (g) – (i), for horizonal, vertical and diagonal, respectively, and three test objects at different depths were used as a test field for

this, with reconstructions as shown in (j) – (l). The combined set of all 3 scan geometries was used for the reconstructed image (m), showing the best preservation of the three objects space and intensities with 30 iterations in each reconstruction. These simulations were carried out once for each in individual graph shown.

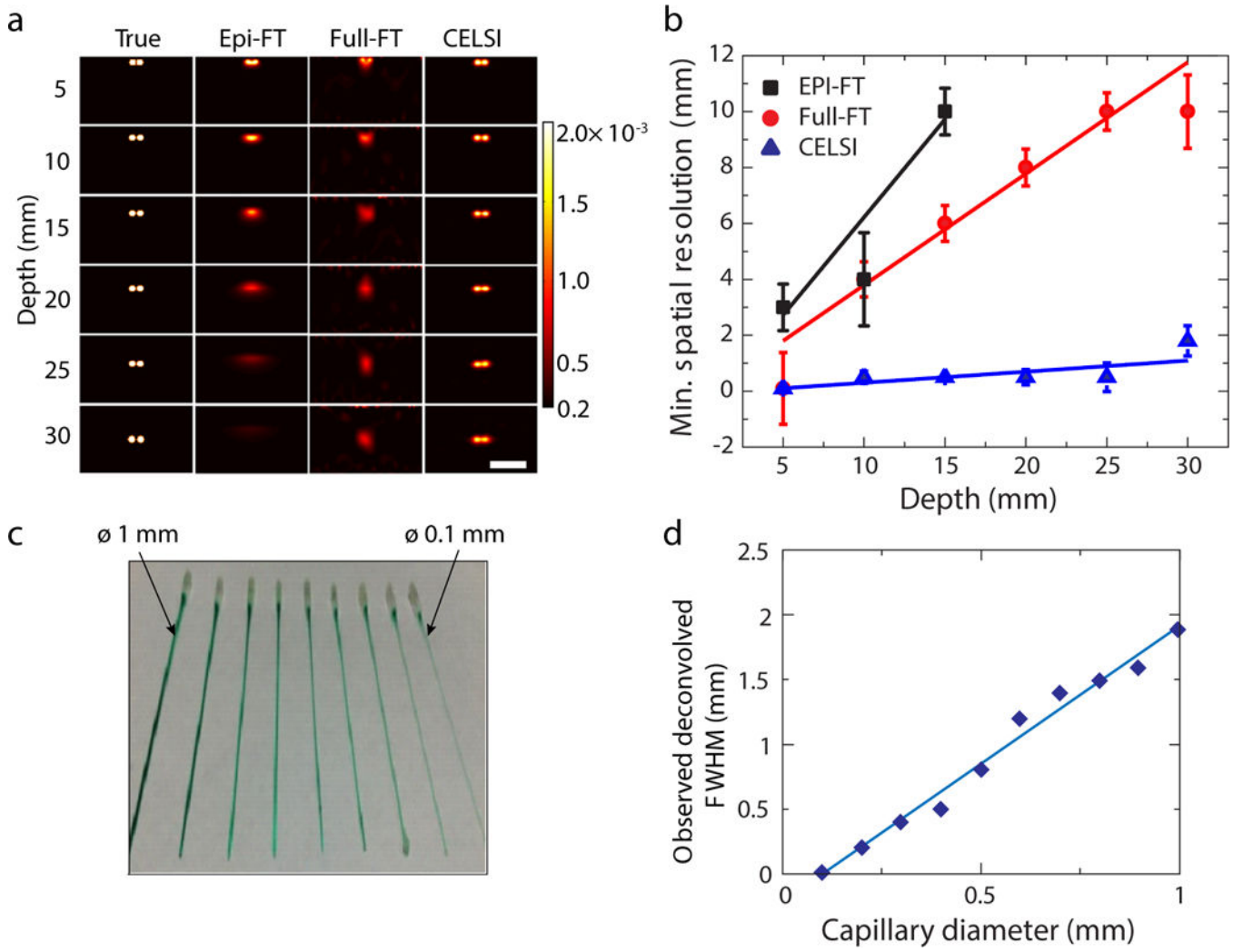

Figure 6.

To establish the theoretical limits to spatial resolution, reconstructed results using CELSI tomography are shown in units of luminescent yield, $\eta\mu_{af}$, in the colorbar, for two inclusions with varied edge-to-edge distance in different depths are shown, (a). The white scale bar in the bottom right is 30 mm. These simulations were carried out once for each location of the pair of 5mm diameter, 50 μM PtG4, inclusions. At each depth, the minimum resolvable distance was estimated and plotted in (b), for epi-illumination fluorescence tomography, diffuse fluorescence tomography, and CESLI tomography. Capillaries filled with PtG4 are shown (c) varying from 0.1mm diameter up to 1.0 mm diameter, and were embedded into a tissue equivalent phantom, and a sheet beam scanned laterally to extract the FWHM for each sized tube (d). Each data point reports a single measurement, and fitting was completed with r^2>0.9 for each sample.

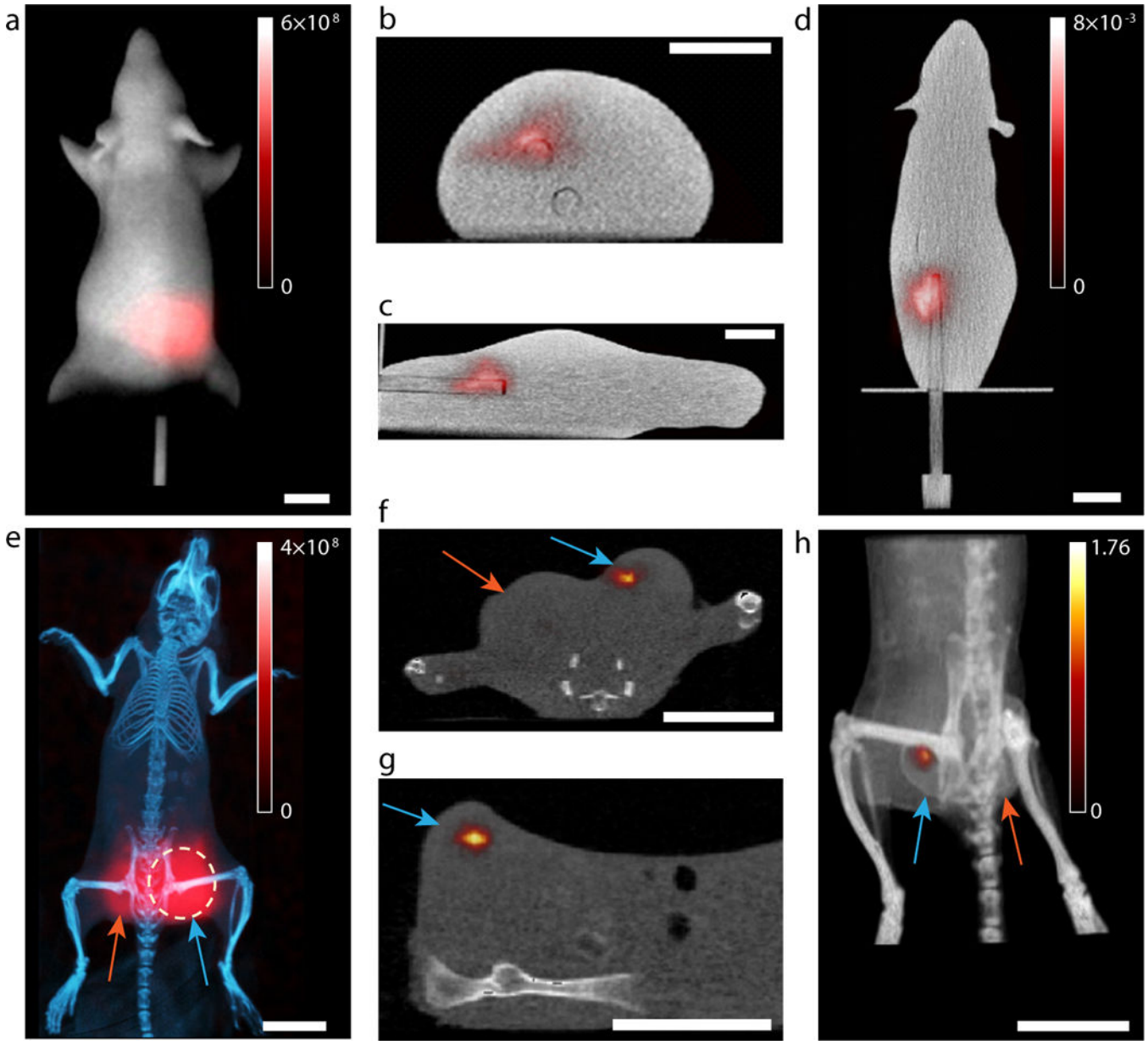

Figure 7.

The phantom experiments shown as measured once. (a) The luminescent yield images are overlaid on the top surface of the microCT image, in colorbar units of photons/cm^2/s, and the reconstructed images shown with 3 orthogonal views, axial (b), sagittal (c) and transverse (d) with the colorbar reporting values for (b)-(d) in units of $\eta\mu_{af}$. The in vivo imaging study is shown from a single animal, with an x-ray CT scan and a summed intensity projection image of the luminescence overlaid on the color-coded CT scan (e) in colorbar units of photons/cm^2/s. Then CELSI tomographic data is overlaid on the high resolution microCT images for axial (f), sagittal (g) and 3D perspective (g) views of the reconstruction. The location of the two MDA-MB-231 tumors grown on the hind flanks are shown by arrows, with 50 nmol PtG4 injected into the tumor with a blue arrow, and 10 nmol PtG4 was

injected into the tumor with the orange arrow, and the entire body of the animal was scanned and reconstructed with CELSI. The reconstructed image shows recovery of the high concentration injection while the lower concentration injection is not recovered, to illustrate the detectable limit is in the range of tens of nanomoles. (A full rotating 3D video of this mouse is available in the Supplementary Information, Section S.7)

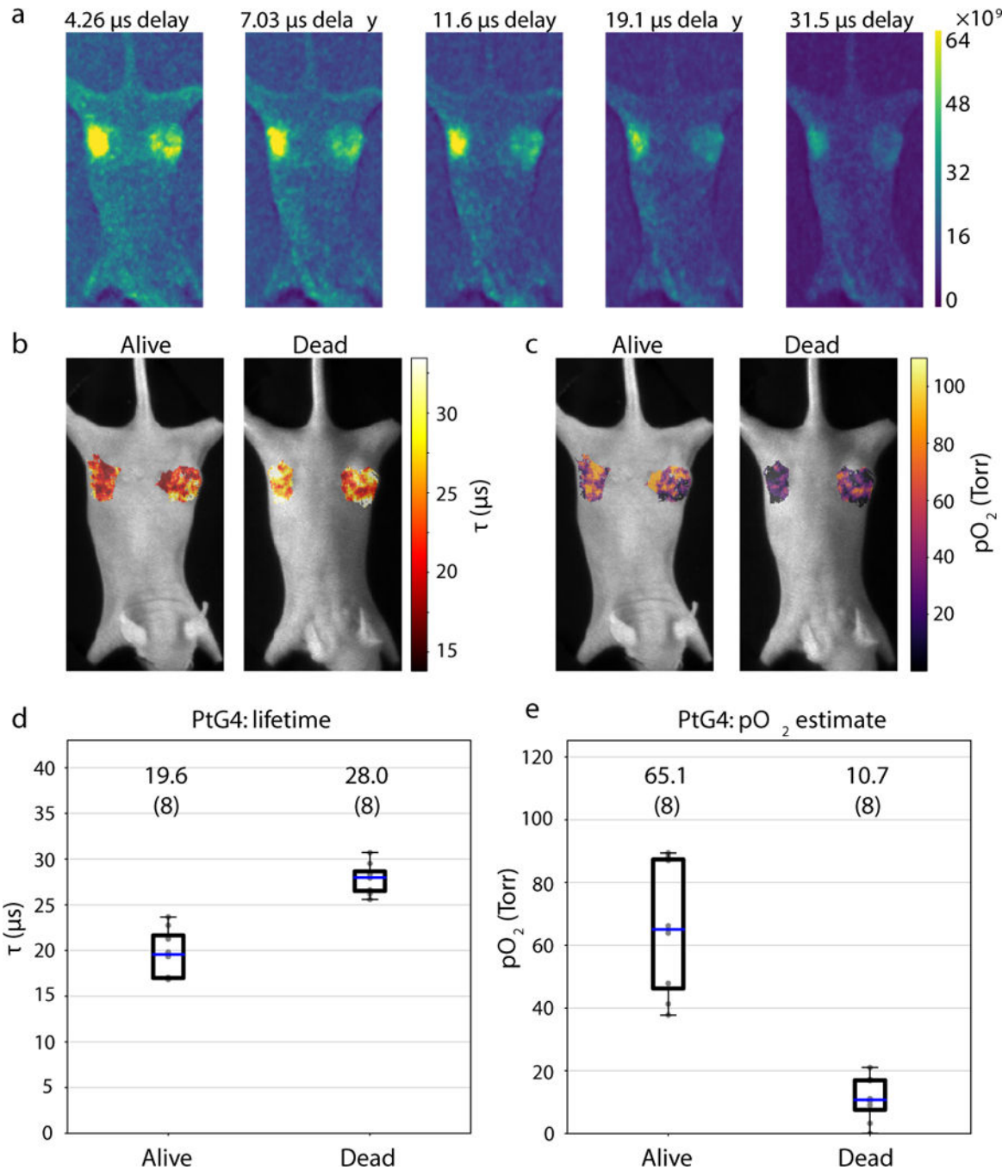

Figure 8.

Nude mice with subcutaneous breast adenocarcinomas (MDA-MB-231) were injected with 50uL of 25uM PtG4 in each tumor and imaged. In (a) Maximum intensity projection (MIP) images of CELSI are shown with increasing delays after radiation pulse, with color bar in photons/cm^2/s, and (b) the pixel-wise lifetimes (τ) estimated alive, and after sacrifice as a low pO_2 control. These were used to (c) calculate pO_2 maps via the Stern-Volmer relationship. In (d) box-plots show lifetime estimates for all tumors (n=8), and (e) shows the calculated pO_2 estimates for these (n=8). Measurement scans were acquired once for each

animal. (A video of a single scan sequence is available in the Supplementary Information, Section S.7).